Stability of ironcrystal structures at 0.3–1.5 TPa

B.K. Godwal [a,*], F. González-Cataldo [b], A.K. Verma [c], Lars Stixrude [d], Raymond Jeanloz [a,e]

[a] Earth & Planetary Science, University of California, Berkeley, CA 94720-4767, USA
[b] Group of Nano Materials, Departamento de Física, Facultad de Ciencias, Universidad de Chile, Casilla 653, Santiago, Chile
[c] High Pressure & Synchrotron Radiation Physics Division, Bhabha Atomic Research Centre, Trombay, Mumbai, India 400084
[d] Department of Earth Sciences, University College London, Gower Street, London, WC1E 6BT, United Kingdom
[e] Miller Institute for Basic Research in Science and Department of Astronomy, University of California, Berkeley, CA 94720, USA

ARTICLE INFO

ABSTRACT

Ab initio molecular dynamics simulations carried out for tetragonal and orthorhombic distortions of iron closely follow the results of static-lattice electronic-structure calculations in revealing that the body-centered cubic (bcc) phase of Fe is mechanically unstable at pressures of 0.3–1.5 TPa and temperatures up to 7000 K. Crystal-structural instabilities originate in the static lattice for the bcc configuration, and are consistent with recent results from both static and dynamic high-pressure experiments. Both theory and experiment thus show that the close-packed (hexagonal, hcp and face-centered cubic, fcc) crystal structures of iron are those relevant to the cores of Earth-like planets.

© 2014 Elsevier B.V. All rights reserved.

1. Introduction

There has been longstanding controversy about the stable crystalline phases of iron at pressures of 300–1500 GPa (0.3–1.5 TPa $\approx$ 3–15 Mbar), with claims that the body-centered cubic (bcc) structure may be stable at temperatures close to the melting point (Brown and McQueen, 1986; Boehler, 1993; Dubrowinsky et al., 2007; Ross et al., 1990; Vocadlo et al., 2003, 2008; Belonoshko et al., 2003, 2006, 2007, 2008, 2009; Luo et al., 2010; Kong et al., 2012; Bouchet et al., 2013). The theoretical rationale is that entropy associated with atomic vibrations might stabilize the bcc relative to close-packed structures at combined high pressures and temperatures. Recent experiments do not reveal evidence for the bcc phase at these conditions, but instead point to the hexagonal close-packed (hcp) structure being stable, these results having implications for disciplines ranging from applied physics and engineering to the geophysics of planetary cores (Tateno et al., 2010, 2012; Ping et al., 2013; Anzellini et al., 2013; Wang et al., 2013). In particular, the discovery of large numbers of extrasolar planets provides motivation for understanding the properties of Fe – a key planetary core-forming element – at high pressures and temperatures (Seager et al., 2007; Petigura et al., 2013).

Here we review theoretical evidence pointing to bcc iron being unstable at 0.3–1.5 TPa based on first-principles calculations, both for the static lattice and via molecular dynamics. The strongest arguments for high temperature stabilizing bcc Fe resulted from use of classical many-body potentials (Belonoshko et al., 2003, 2007, 2008, 2009), and misinterpretation of the requirements of mechanical stability in prior simulations (Vocadlo et al., 2003; Belonoshko et al., 2006; Bouchet et al., 2013). We show that these studies suffer from the use of approximate potentials, the accuracy of which is untested, and from focusing on the hydrostatic nature of the stresses for inferring mechanical stability. However, hydrostatic equilibrium inferred from inspection of stresses does not need to correspond to a free energy minimum; it can instead be due to a local maximum, with the unit cell metastable with respect to a finite tetragonal strain. On this last point, Vocadlo et al.'s (2008) ab initio free-energy calculations for the bcc phase do consider tetragonal distortions, and find bcc Fe becoming mechanically stable above 6000 K at Earth-core density (vs. 4500 K found in a previous paper, Vocadlo et al., 2003). However, this study lacks

the necessary accuracy and convergence. Similarly, Bouchet et al.'s (2013) work is inadequate in using hydrostatic equilibrium to determine mechanical stability of the *bcc* structure. We find instead, from more accurate and fully converged *ab-initio* calculations, that the *bcc* phase of Fe is unstable to temperatures of 7000 K at inner-core densities.

Ironically, recent theoretical work shows that the *bcc* structure is in fact stabilized again at much higher pressures, above 20 TPa; however, this is because of the engagement of core electrons in the interatomic bonding of iron (Pickard and Needs, 2009; Stixrude, 2012). Thus, both theory and experiment confirm that Fe forms in a close-packed structure at the conditions of Earth-like planetary interiors.

2. Electronic structure calculations

Electronic-structure based total-energy calculations were carried out using the projector augmented-wave (PAW) method as implemented in VASP (Kresse and Joubert, 1999; Kresse and Furthmuller, 1996), based on density-functional theory (DFT) with the generalized-gradient approximation (GGA) of Perdew, Burke and Ernzerhof (GGA-PBE) (Perdew et al., 1996). The PAW method is closely related to use of ultra-soft pseudopotentials, and gives results that agree with those of all-electron calculations. The $3p$ and $4s$ semi-core electrons were taken in their valence configuration in generating the pseudopotential, and an energy cutoff of 350 eV was used for the plane-wave expansion. The simulations are confined to the Born–Oppenheimer surface, and the effect of finite temperature on the electronic structure is included through Mermin's formalism (Mermin, 1965). We implemented an $18 \times 18 \times 18$ Monkhorst–Pack **k**-point mesh (Monkhorst and Pack, 1976), and Brillouin-zone (BZ) integration was carried out with the linear tetrahedral method (Blöchl et al., 1994).

For tracking iron phases along the Bain transformation path we used a body centered tetragonal cell (*bct*: space group I4/mmm) at a volume of 7.2 Å^3/atom, and for the *bcc–hcp* transition path under orthorhombic distortions we used a 4 atom orthorhombic cell (space group Cmcm, with lattice vectors a, b and c), which accommodated *fcc* (face-centered cubic), *hcp* and *bcc* structures, and allowed for changes in the cell shape and relaxation of internal degrees of freedom (see Online Suppl. Material, Section S1 and Table S1).

3. Results of electronic structure calculations

The total energy was calculated for tetragonal and orthorhombic strains with varying c/a (Bain path), as well as b/a, c/a along with y parameters (see Online Suppl. Material, Figs. S1 and S2). Under tetragonal distortions, the *bcc* phase occupies a local energy maximum at $b/a = c/a = 1$, and minima corresponding to the *fcc* phase are at $c/a = \sqrt{2}$, $b/a = 1$; $b/a = \sqrt{2}$, $c/a = 1$; and $c/a = b/a = 1/\sqrt{2}$. The *bct* structure is located at a saddle point at $c/a = 0.9$ and $b/a = 1.0$, from which the total energy decreases as the b/a ratio is changed. An energy surface with similar topology is well known in other transition metals (Mehl et al., 2004), and our results agree with *ab initio* re-determinations of the b/a–c/a energy surface (Mikhaylushkin et al., 2009) (Online Suppl. Material, Section S1). The total-energy calculations under orthorhombic distortions further reveal the stability of the *fcc* ($b/a = c/a = 1$) and *hcp* ($b/a = 1.732$, $c/a = 1.633$) structures (Online Suppl. Material, Fig. S2). The *bcc* structure ($b/a = c/a = \sqrt{2}$) is clearly unstable, but lies close to the energy minimum defining the stability region of *hcp* (Online Suppl. Material, Fig. S2). Thus, the electronic structure-based total-energy calculations for static ions document the stability of close-packed (*hcp* and *fcc*) structures, in contrast to the *bcc* phase that is seen to be unstable under both tetragonal and orthorhombic distortions.

4. Molecular dynamic simulations

To check the results of the total-energy calculations for static ions, we performed *ab initio* molecular dynamics (AIMD) simulations for tetragonal (Vocadlo et al., 2008; Belonoshko et al., 2006) and orthorhombic strains (Online Suppl. Material, Section S2). AIMD is more time consuming than molecular dynamics based on semi-empirical classical potentials, but has the important advantage of making no *a priori* assumptions concerning the nature of the charge density, electronic structure or bonding. Our simulations are performed in the *NVT* ensemble (*N*, number of atoms; *V*, volume; *T*, temperature), with a Nosé thermostat (Nose, 1984) and a supercell containing 128 ($4 \times 4 \times 4$ *bcc* and *bct* unit cells) and 180 ($5 \times 3 \times 3$ orthorhombic unit cells) atoms for tetragonal and orthorhombic distortions respectively. Both tetragonal and orthorhombic strains allowed for changes in the cell shape and relaxation of internal degrees of freedom. We sample the Brillouin zone on a $2 \times 2 \times 2$ **k**-point mesh, and assume thermal equilibrium between ions and electrons via the Mermin functional (Mermin, 1965) (i.e., we set the electronic temperature $T_{el} = T$). The calculations were carried out for a volume of 7.2 Å^3/atom for temperatures varying from 5500 to 7000 K. Using a time step of 1 fs, we find that 15 000 time steps ($\approx$15 ps) yield converged values of the stress tensor, with the final 10 ps used for accumulating averages. The uncertainty in the components of the stress tensor due to thermal fluctuations is evaluated with the blocking method (Adams and Oganov, 2006; Flyvbjerg and Petersen, 1989). Although the possibility of magnetism is considered in recent work of Ruban et al. (2013), all our calculations are based on the PAW approach described above and are non-spin polarized, as previous calculations have shown that the phases of iron are non-magnetic for the pressure–temperature conditions we have considered (Vocadlo et al., 2003; Stixrude et al., 1994). AIMD calculations under tetragonal distortions were carried out for c/a values of 0.9 to 1.2 and for orthorhombic distortions for points A, B, C and D defined as follows: point A ($b/a = 1.45$, $c/a = 1.42$) is close to *bcc*, while B ($b/a = 1.50$, $c/a = 1.45$) and C ($b/a = 1.573$, $c/a = 1.523$) are distorted toward *hcp*; point D ($b/a = 1.135$, $c/a = 1.125$) corresponds to distortion toward *fcc* (Online Suppl. Material, Table S3 and Fig. S4).

5. Results of stability analysis using molecular dynamic simulations

5.1. Tetragonal distortion

Mean square displacements (MSD) for tetragonal strains (Fig. 1, left panel) show motion of atoms in the Z direction increasing with increase in c/a ratio (X, Y and Z correspond to a, b and c directions (Online Suppl. Material, Section S2). The stresses (S_{ij} with $i, j = x, y$, or z) as a function of time (Fig. 2) become anisotropic for c/a values deviating on either side of the 1 value for *bcc*, towards either *bct* or *fcc*. This is due to tetragonal distortion; and with no distortion ($c/a = 1$) the stresses are isotropic, implying they are hydrostatic in the simulation cell. Development of anisotropic stresses results in instability in the longitudinal stress, $S_L = S_{zz} - (S_{xx} + S_{yy})/2$, which is related to the shear elastic constant B_S. $S_L = 0$ and $B_S > 0$ provide the necessary and sufficient conditions for mechanical stability (Online Suppl. Material Eqs. S4, S5 in Section II). By analogy with S_L, we also compute shear-stress instabilities ($S_S = S_{zx} - (S_{xy} + S_{yz})/2$) that we believe to be responsible for the *bcc–hcp* transition away from the Bain path. In strained configurations, the stress tensor
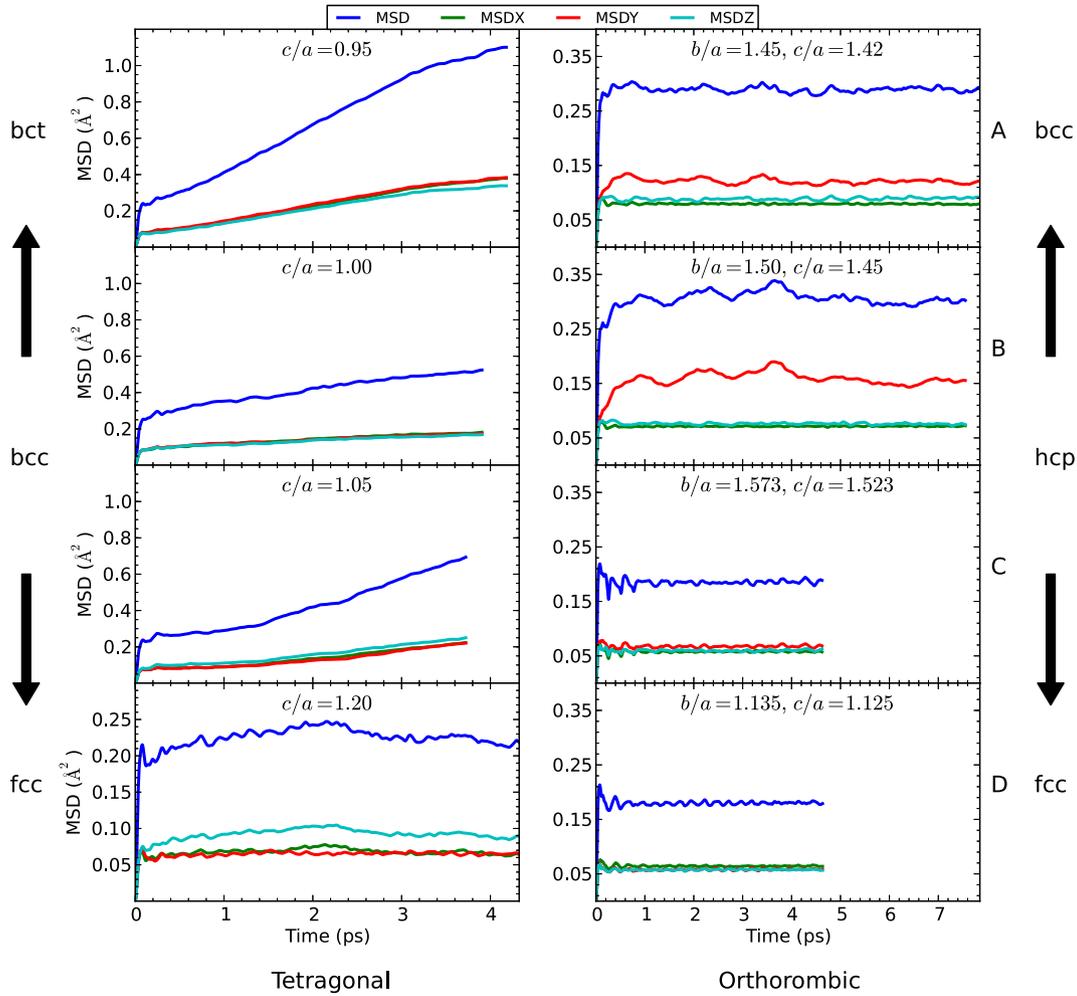
Fig. 1. Mean square displacements (MSD) of atoms along *X*, *Y* and *Z* directions, and the resultant MSD for tetragonal (left panel) and orthorhombic (right panel) distortions.

is anisotropic, as demonstrated by the values of the longitudinal stress anisotropy (Figs. 3 and 4), which decreases monotonically with increasing $\delta = (c/a)^{2/3} - 1$ from $c/a = 0.95$ to $c/a = 1.05$ (Online Suppl. Material, Fig. S3). There is thus no restoring force acting against tetragonal strain: S_{zz} becomes more negative as the *c*-axis is stretched, corresponding to a driving force acting to further stretch the *c*-axis. At $\delta = 0$ ($c/a = 1$) the stress tensor is isotropic, in agreement with previous *ab initio* molecular dynamics simulations (Vocadlo et al., 2003; Belonoshko et al., 2006; Bouchet et al., 2013).

Detailed analysis reveals that *bcc* iron violates the Born stability criterion for the shear modulus (Online Suppl. Material, Section S2-II and Eq. S5), which has not always been examined in previous *ab initio* molecular dynamics studies. We find that $B_S = -50$ GPa for $c/a = 1.05$, clearly documenting instability (Online Suppl. Material, Table S2 and Eq. S3 in Section S2-II). This disagrees with previous *ab initio* results giving $(B_{11} - B_{12}) > 0$, but the calculations were for much smaller systems (54 atoms) and we infer that they were under-converged (Vocadlo, 2007) (Suppl. Material, Section S2).

In addition, *bcc* iron has erroneously been claimed stable due to the calculations finding the stress tensor to be isotropic for $c/a = 1$, $S_L(\delta = 0) = 0$: this condition guarantees only that *bcc* iron occupies a local extremum on the energy surface (Vocadlo et al., 2003; Belonoshko et al., 2006; Bouchet et al., 2013). Later work on the stability of *bcc* iron under tetragonal strain found significantly different results when using a 128 atom cell and a single **k** point,

including mechanical stability of *bcc* Fe at 6000 K with 64 atom cell (Vocadlo et al., 2008). This is in accord with the present, more extensive simulation, where we also find that shear anisotropy develops upon application of tetragonal strain, a feature that is not apparent in low-temperature calculations based on the primitive unit cell. In Fig. 4, the stress anisotropy obtained from electronic structure calculations (lower panel) can be compared with results from AIMD simulations (upper panel). The shear-stress anisotropy is smaller than the longitudinal anisotropy (mostly positive) for c/a values up to 1.2 (Fig. 3), demonstrating a further mechanical instability of *bcc* iron that has not been previously recognized.

Other studies claiming mechanical stability of *bcc* iron are not based on *ab initio* molecular dynamics, but instead on an embedded atom model (EAM) potential that is fit to a limited number of *ab initio* results (Vocadlo et al., 2003). Results based on EAM (Belonoshko et al., 2003) cannot be considered reliable, among other reasons, because they predict *bcc* to have the lowest Gibbs free energy at the conditions considered here, in disagreement with *ab initio* calculations showing that *hcp* is in fact most stable (Vocadlo et al., 2003). Therefore, past studies claiming stability of *bcc* Fe suffered from (i) misinterpretation of the requirements for mechanical stability (stability inferred only from isotropy of the stress tensor for *bcc*) and/or (ii) the use of classical many-body potentials, the accuracy of which are untested for documenting mechanical stability of *bcc* iron.
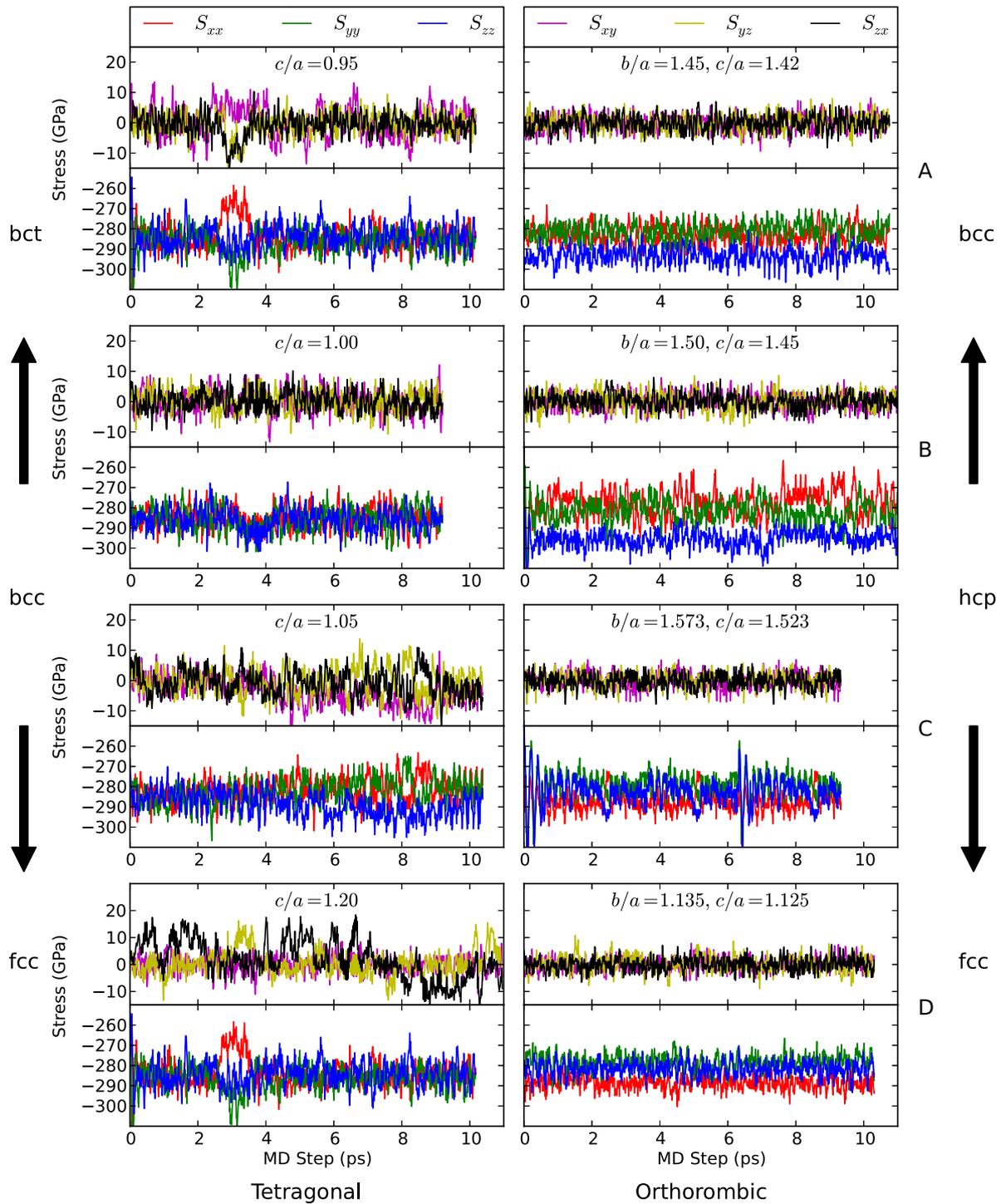
Fig. 2. Variation of stress tensor components with time for tetragonal (left panel) and orthorhombic (right panel) distortions.

5.2. Orthorhombic distortion

For orthorhombic strains, MSD in the Y direction increase considerably for distortion from point A to B and decrease for point C, which is close to *hcp* (Fig. 1, right panel). For distortion toward *fcc* (D), the MSD in the X direction are larger than in Y and Z directions. However, there is no notable difference in the MSD of atoms in any directions for *bcc*. Although point A (right panel) is close to *bcc*, we notice large atomic motion in the Y direction, as compared to the Z direction for $c/a = 1.05$ (left panel, Fig. 1), indicating stronger instability for orthorhombic distortions. The longitudinal stress anisotropy increases for orthorhombic distortions away from

bcc ($b/a = c/a = \sqrt{2}$) toward A and B: in Fig. 2 (right column), the diagonal elements of the stress tensor (lower panels) show greater spread in values near *bcc* (point A and especially point B) than for closed-packed structures points (C and D, corresponding nearly to *hcp* and *fcc*). The upper panels in Fig. 2 show the off-diagonal elements. We also note that the off-diagonal elements of the stress tensor under tetragonal distortion show larger anisotropy (almost by a factor of 10) ascompared with the values for orthorhombic distortion.

For orthorhombic distortions, we compute the quantities $S_c = S_{zz} - S_{xx}$ and $S_b = S_{yy} - S_{xx}$ from the diagonal elements of the
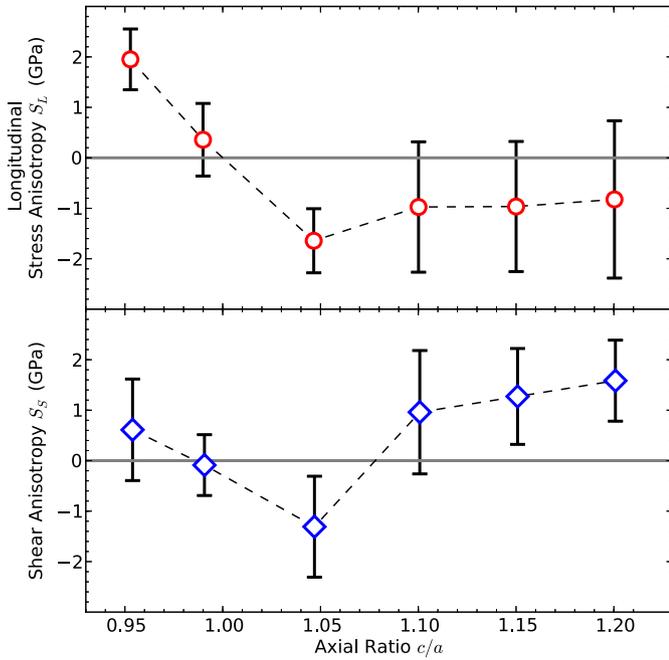
Fig. 3. Comparison of longitudinal-stress anisotropy with shear-stress anisotropy as a function of c/a ratio. Shear-stress instabilities are smaller than longitudinal-stress instabilities, mostly positive within the associated uncertainties. We point out that shear instabilities are the outcome of MD simulations, and are absent in electronic-structure total-energy calculations along the Bainpath (Online Suppl. Material, Fig. S3).

Fig. 4. (Top) Variation of longitudinal elastic anisotropy with tetragonal strain from *ab initio* molecular dynamics simulations (*red symbols*) as compared with the result for the static lattice with $T_{el} = 5500$ K (*green line*). The open diamonds represent the results of Vocadlo et al. (2008) for a 128 atom cell sampled at a single **k**-point. (Bottom) Computed free energy (*top*, plotted relative to *fcc* energy) and stress anisotropy S_L (*bottom*) of iron along the isochoric Bain path at a volume of 7.2 Å³/atom for the static lattice, and for electrons at $T_{el} = 0$ (*blue*) and $T_{el} = 5500$ K (*green squares*). The values of the c/a ratio corresponding to the *bcc* (1.0) and *fcc* ($\sqrt{2}$) structures are indicated by vertical black lines. The yellowshading shows the range of c/a values that violate the Born stability criterion for $T_{el} = 5500$ K. (For interpretation of the references to color in this figure legend, the reader is referred to the web version of this article.)

stress tensor, and resulting strains $e_c = \varepsilon_c - \varepsilon_a$ and $e_b = \varepsilon_b - \varepsilon_a$ (due to stretching toward *hcp* and *fcc*) relative to the corresponding *bcc* supercell (for $b/a = c/a = \sqrt{2}$: Online Suppl. Material, Section S2-III and Table S3). We determine stability by the sign of the stress–strain products $S_c \cdot e_c$, $S_b \cdot e_b$, with positive values indicating stability and the stresses tend to restore the structure; if the products are negative, then the applied strain is further enhanced and the structure is unstable. For distortions of *bcc* toward *hcp*, *A* ($b/a = 1.45$, $c/a = 1.42$), *B* ($b/a = 1.5$, $c/a = 1.45$), we find positive values for both e_c and e_b and negative values for both S_c and S_b: the structures are therefore mechanically unstable (Online Suppl. Material, Section S2-III and Eq. S7). We found that sampling the Brillouin zone on at least a $2 \times 2 \times 2$ **k**-point mesh was essential in arriving at these conclusions.

5.3. Structure analysis for tetragonal and orthorhombic distortions

In order to determine the structure resulting from this instability, we use the molecular dynamics program LPMD (http://www.lpmd.cl) (Davis et al., 2010) to perform a common neighbor analysis (Honeycutt and Andersen, 1987) that allows us to distinguish among different structures produced from the molecular dynamics (MD) simulations (Online Suppl. Material, Section S2-IV, Fig. S5). We used the thermodynamically equilibrated structure represented by the final MD step, the resulting patterns for tetragonal and orthorhombic distortions being shown in the supplementary material (Online Suppl. Material, Section S2-IV, Fig. S6). As the final step MD simulations failed to provide any structure we generated time-averaged structures for each case from the average positions of individual atoms over the entire MD simulation, taking into account the effect of periodic boundary conditions (Online Suppl. Material, Section S2-IV). We noticed that for tetragonal distortions of $c/a = 0.95$ and 1.05 the time-averaged structures have a majority of neighboring pairs consistent with *bcc* and *hcp* structures, respectively (Online Suppl. Material, Fig. S7 and Table S7). Orthorhombic distortions yield time-averaged structure corresponding to *bcc* for
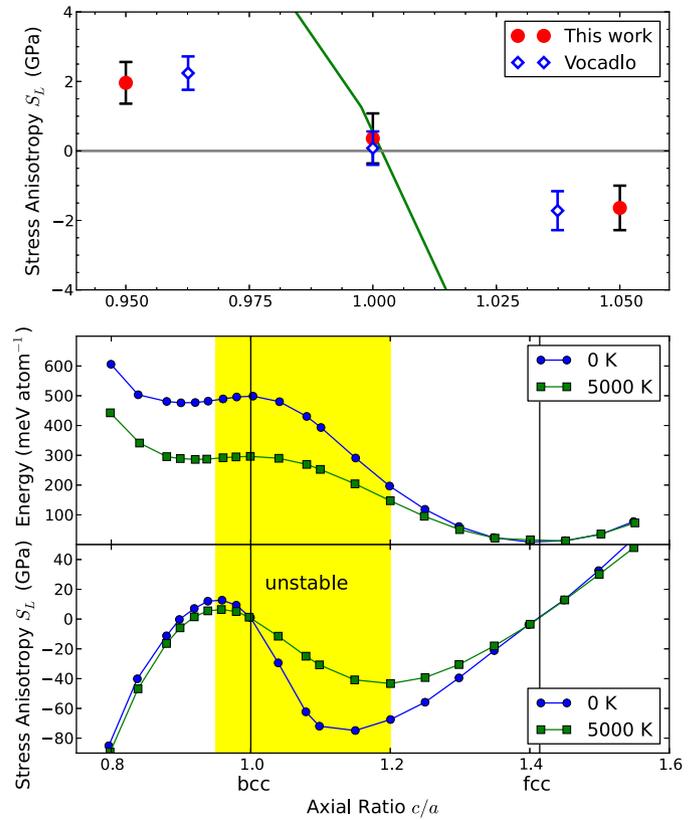
point *A* and an unknown structure for point *B* (Online Suppl. Material, Fig. S8 and Table S7). The atoms had large forces on them in all these cases, and it was necessary to either quench or relax the internal degrees of freedom of the structures. Hence, we investigated the distortion of *bcc* iron under tetragonal and orthorhombic distortions by quenching the final time-step of our AIMD simulation. During the quenching process, the total energy was minimized by adjusting the atomic positions while keeping the supercell fixed in volume. The quenched structures reveal displacements in mean-atomic positions away from *bcc* sites (Fig. 5) and along the most unstable zone-boundary mode eigenvector, which occurs at the *N*-point and relates the *bcc* structure to the *hcp* structure (Wang and Ingalls, 1998; Grimvall et al., 2012).

Quenching at $c/a = 0.95$ and 1.05 for tetragonal distortion and for orthorhombic distortions *A* and *B* led to the final *hcp* structure (Online Suppl. Material, Figs. S7 and S8). For tetragonal distortions up to $c/a = 1.2$, all the time-averaged structures were *bcc* (except $c/a = 1.05$, which was *hcp*), and analysis of the relaxed or quenched final MD step yielded the *hcp* structure. We feel the existence of shear stress instabilities might be the reason for obtaining the *hcp* structure, which is not on the *bcc–fcc* transition along the Bain path. The time-averaged structures for points *C* and *D* under orthorhombic distortion are *hcp* (50% each of 4–2–1 and 4–2–2 types of pairs from the common neighbor analysis) and *fcc* (100% 4–2–2 types of pairs), respectively (Online Suppl. Material,
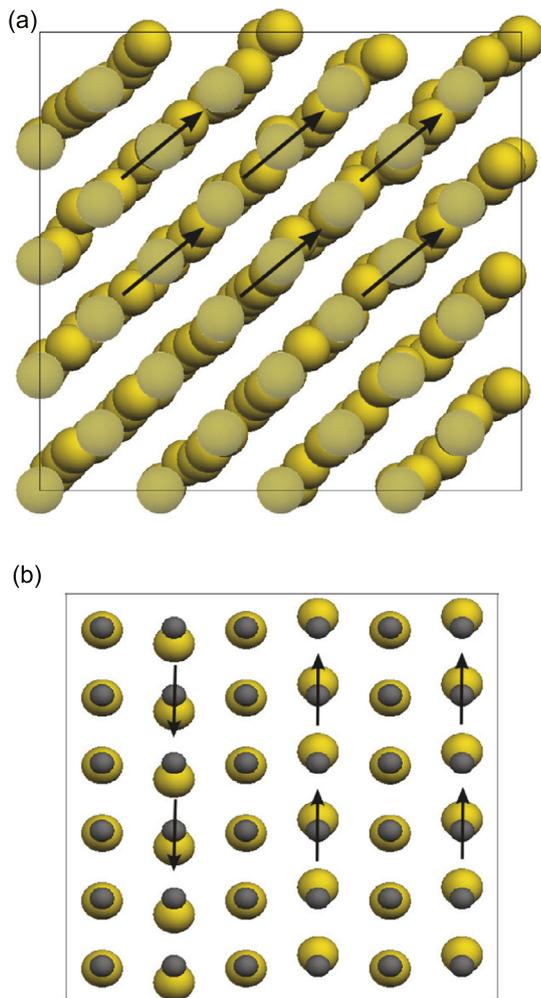
(a)

(b)

Fig. 5. Representation of the structure of Fe in the Y–Z plane resulting from quenching the final time step of the MD run (a) for tetragonal distortion $c/a = 1.05$, and (b) for orthorhombic distorted point A. Arrows show the pattern of atomic motions from ideal *bcc* sites for tetragonal distortion for $c/a = 1.05$ and for orthorhombic distorted point B (*grey*) to relaxed atomic positions (*yellow*). (For interpretation of the references to color in this figure legend, the reader is referred to the web version of this article.)

Section S2-IV). The atoms had large residual forces, and quenching or relaxing the final MD step recovered the respective *hcp* and *fcc* structures.

5.4. Possibility of bcc phase at high temperatures and densities

We investigated the stability of bcc iron at temperatures higher than 5500 K and inner-core densities. *Ab initio* molecular dynamic (AIMD) calculations for tetragonal distortion ($c/a = 1.05$) and orthorhombic distortion (point A) show the stress variation to be

highly anisotropic at 7000 K (Online Suppl. Material, Fig. S9, Section V). The stress stability analysis (Suppl. Material, Section S2 II) carried out for tetragonal distortion ($c/a = 1.05$ at 7000 K) yields a negative shear modulus of -82 GPa. Applying the stress stability analysis for the orthorhombic distortion (point A) at 7000 K gives negative $S_c \cdot e_c$ and $S_b \cdot e_b$ products (Suppl. Material, Section S2-III). In short, the *bcc* phase is unstable up to temperatures of 7000 K at Earth inner-core density (structural details provided in Suppl. Material, Section V).

We carried out AIMD simulations for tetragonal distortions along the isochoric Bain paths for the density and temperature conditions reported in the paper by Bouchet et al. (2013), comparing results for a $2 \times 2 \times 2$ **k**-point mesh with those for only the Γ-point. Our PAW potentials include 3s, 3p, 3d and 4s states as valence electrons, with cutoff radii and cutoff energies the same as the values used in Bouchet et al. (2013). We find the stresses becoming anisotropic for tetragonal distortions on either side of $c/a = 1$ for densities of 16, 18 and 20 g/cm³ at temperatures above those that Bouchet et al. (2013) inferred the *bcc* structure to be stable (see Fig. 6 for the evolution of stresses as a function of tetragonal distortion at densities of 18 g/cm³ and 20 g/cm³ at temperatures of 6000 K and 7000 K, respectively). The stresses were averaged over the simulation time, the time-averaged diagonal components of stress being provided in Table 1. The longitudinal stress anisotropy S_L is close to zero, within the uncertainties in stress (Table 1). However $S_L > 0$ for $c/a < 1$, and $S_L < 0$ for $c/a > 1$, which is exactly opposite the requirement for stability. The shear modulus is therefore negative, violating the second stability condition ($B_s > 0$, Suppl. Material, Section II, Eq. S5). Therefore, our results do not support Bouchet et al.'s (2013) conclusion that the *bcc* phase is stable, as the Born stability criterion is robustly violated for pressures up to 1.5 TPa at 7000 K.

6. Discussion

We find that the mechanical instability of *bcc* iron originates in the static-lattice contribution to the Helmholtz free energy (Fig. 4). For example, a series of static calculations on the Bain path (Online Suppl. Material, Eq. S1) combined with our AIMD results allow us to determine separately the three contributions to the Helmholtz free energy (Stixrude, 2012), $F(V, \delta, T, T_{el}) = F_{st}(V, \delta, T = T_{el} = 0) + \Delta F_{el}(V, \delta, T = 0, T_{el}) + \Delta F_{ph}(V, \delta, T, T_{el})$; from the static lattice and $T_{el} = 0$; from thermal excitation of electronic states ΔF_{el} at finite T_{el}; and from fully anharmonic lattice vibrations ΔF_{ph}. The variation of longitudinal stress S_L with free energy F for the static lattice shows the same mechanical instability seen in the AIMD calculations. At $T = 0$, S_L decreases with increasing δ, which requires $B_S < 0$ and also accounts for the local maximum in the total energy for *bcc* ($\delta = 0$) via $\partial^2 F/\partial \delta^2 = 3V B_S < 0$. The contributions of ΔF_{el} and ΔF_{ph} reduce but do not to eliminate the mechanical instability.

Table 1

Diagonal elements of the stress tensor (negative in sign) averaged over the simulation period, and longitudinal stress instability calculated in the present study for density–temperature values corresponding to Bouchet et al. (2013).

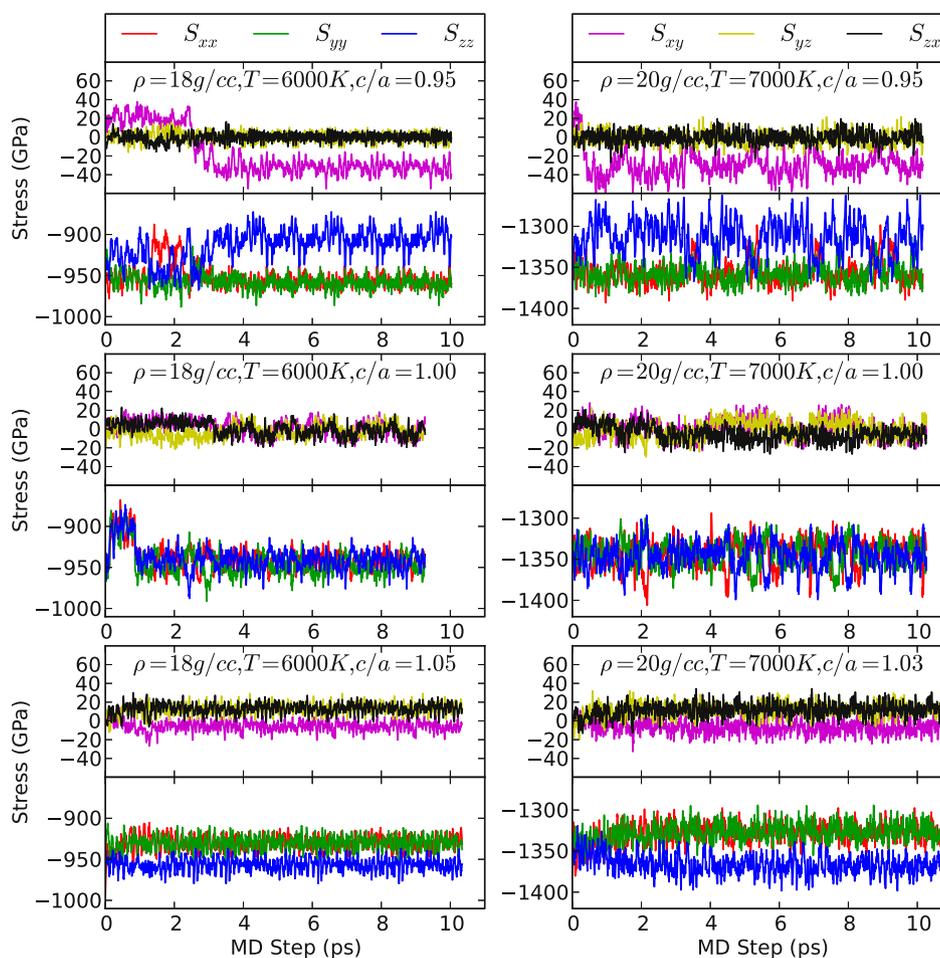| Density, temperature	c/a	S_{XX} (GPa)	S_{YY} (GPa)	S_{ZZ} (GPa)	S_L (GPa)
18 g/cm³, 6000 K	0.95	952.0($\pm$2.5)	957.0($\pm$1.0)	915.0($\pm$4.1)	40.0($\pm$4.3)
	1.0	939.0($\pm$3.0)	944.0($\pm$4.0)	938.0($\pm$3.0)	
	1.05	931.0($\pm$1.2)	930.0($\pm$1.5)	957.0($\pm$1.8)	$-26.0(\pm2)$
20 g/cm³, 7000 K	0.95	1358.0($\pm$3.2)	1358.0($\pm$3.4)	1313.0($\pm$2.9)	45.0($\pm$3.7)
	1.0	1345.0($\pm$0.2)	1343.0($\pm$1.6)	1346.0($\pm$0.9)	
	1.03	1330.0($\pm$2.8)	1329.0($\pm$3)	1365.0($\pm$3.0)	$-35.0(\pm3.6)$

Fig. 6. Variation of stress-tensor components with time for tetragonal distortions for density–temperature conditions corresponding to mechanical stability of *bcc* iron observed by Bouchet et al. (2013).

7. Conclusions

It has been proposed that the *bcc* phase may reappear just below the melting temperature of iron at high pressure (Dubrowinsky et al., 2007; Belonoshko et al., 2003; Ross et al., 1990), perhaps stabilized by anharmonic effects as is the case for *bcc* phases of Ti, Zr and Hf (Souvatzis et al., 2008). Melting is well determined on the Hugoniot of iron (Brown and McQueen, 1986; Nguyen and Holmes, 2004), and recent X-ray diffraction under ramp-compression shows that iron remains in a close-packed structure under dynamic loading to 560 GPa (Ping et al., 2013). Also, laser-heated diamond-cell experiments with online X-ray diffraction suggest that iron remains in the *hcp* structure above 4500 K at 200 GPa (Anzellini et al., 2013). Some experimental support for a *bcc* phase came from work on Fe–10 wt% Ni above 225 GPa and 3400 K (Dubrowinsky et al., 2007), but these results are not supported by later experiments (Tateno et al., 2012; Hirose et al., 2013). Also, studies of Sakai et al. (2011) for Fe (273 GPa, 4490 K), and for Fe–Ni (250 GPa, 2730 K) and Fe–Ni–Si (304 GPa, 2780 K) alloys reveal the *hcp* structure. Recent theoretical work (Γ point only) shows that the presence of up to 6.25 atomic percent Si or S increases the stability of *bcc* Fe at temperatures up to 7000 K, but not enough to actually stabilize this structure (Cui et al., 2013).

In summary, both theory and experiment now document the stability of close-packed (*hcp*) iron at pressures of 0.3–1.5 TPa and for temperatures up to 7000 K. The implication is that the elastic constants of *hcp* Fe should be considered in combination with plausible deformation mechanisms for producing lattice preferred orientation in polycrystals in order to explain the observed seismic structure of Earth's inner core (Stixrude and Cohen, 1995; Steinle-Neumann et al., 1999, 2001; Morelli et al., 1986).

Appendix A. Supplementary material

Supplementary material related to this article can be found online at http://dx.doi.org/10.1016/j.epsl.2014.10.056.

References

Adams, D.J., Oganov, A.R., 2006. Ab initio molecular dynamics study of CaSiO₃ perovskite at *P*–*T* conditions of Earth's lower mantle. Phys. Rev. B 73, 184106.

Anzellini, S., Dewaele, A., Mezouar, M., Loubeyre, P., Morard, G., 2013. Melting of iron at Earth's inner core boundary based on fast X-ray diffraction. Science 340, 464–466.

Belonoshko, A.B., Ahuja, R., Johansson, B., 2003. Stability of the body-centred-cubic phase of iron in the Earth's inner core. Nature 424, 1032–1034.

Belonoshko, A.B., Isaev, E.I., Skorodumova, N.V., Johansson, B., 2006. Stability of the body-centered-tetragonal phase of Fe at high pressure: ground-state energies, phonon spectra, and molecular dynamics simulations. Phys. Rev. B 74, 214102.

Belonoshko, A., Skorodumova, N.V., Davis, S., Osiptsov, A.N., Rosengren, A., Johansson, B., 2007. Origin of the low rigidity of the Earth's inner core. Science 316 (5831), 1603–1605.

Belonoshko, A.B., Skorodumova, N.V., Rosengren, A., Johansson, B., 2008. Elastic anisotropy of Earth's inner core. Science 319, 797–800.

Belonoshko, A.B., Derlet, P.M., Mikhaylushkin, A.S., Simak, S.I., Hellman, O., Burakovsky, L., Swift, D.C., Johansson, B., 2009. Quenching of bcc-Fe from high to room temperature at high-pressure conditions: a molecular dynamics simulation. New J. Phys. 11 (9), 093039.

Blöchl, P.E., Jespen, O., Andersen, O.K., 1994. Improved tetrahedron method for Brillouin-zone integrations. Phys. Rev. B 49, 16223–16233.

Boehler, R., 1993. Temperatures in the Earth's core from melting-point measurements of iron at high static pressures. Nature 363, 534.

Bouchet, J., Mazevet, S., Morard, G., Guyot, F., Musella, R., 2013. Ab initio equation of state of iron up to 1500 GPa. Phys. Rev. B 87, 094102.

Brown, J.M., McQueen, R.G., 1986. Phase transitions, Gruneisen parameter, and elasticity for shocked iron between 77 GPa and 400 GPa. J. Geophys. Res., Solid Earth 91, 7485–7494.

Cui, H., Zhang, Z., Zhang, Y., 2013. The effect of Si and S on the stability of bcc iron with respect to tetragonal strain at the Earth's inner core conditions. Geophys. Res. Lett. 40, 2958–2962.

Davis, S., Loyola, C., Gonzalez, F., Peralta, J., 2010. Las Palmeras Molecular dynamics: a flexible and modular molecular dynamics code. Comput. Phys. Commun. 181, 2126–2139.

Dubrowinsky, L., Dubrovinskaia, N., Narygina, O., Kantor, I., Kuznetzov, A., Prakapenka, V.B., Vitos, L., Johansson, B., Mikhaylushkin, A.S., Simak, S.I., Abrikosov, I.A., 2007. Body centered cubic iron nickel alloy in Earth's core. Science 316, 1880–1883.

Flyvbjerg, H., Petersen, H.G., 1989. Error estimates on averages of correlated data. J. Chem. Phys. 91, 461–466.

Grimvall, G., Magyari-Kope, B., Ozolins, V., Persson, K.A., 2012. Lattice instabilities in metallic elements. Rev. Mod. Phys. 84, 945–986.

Hirose, K., Labrosse, S., Hernlund, J., 2013. Composition and state of the core. Annu. Rev. Earth Planet. Sci. 41, 657–691.

Honeycutt, J.D., Andersen, H.C., 1987. Molecular dynamics study of melting and freezing of Small Lennard–Jones clusters. J. Phys. Chem. 91, 4950–4963.

Kong, L.T., Li, J.F., Shi, Q.W., Huang, H.J., Zhao, K., 2012. Dynamical stability of iron, under high-temperature and high-pressure conditions. Europhys. Lett. 97 (5), 56004.

Kresse, G., Furthmuller, J., 1996. Efficient iterative schemes for ab initio total-energy calculations using a plane-wave basis set. Phys. Rev. B 54, 11169.

Kresse, G., Joubert, D., 1999. From ultrasoft pseudopotentials to the projector augmented method. Phys. Rev. B 59, 1758–1775.

Luo, W., Johansson, B., Eriksson, O., Arapan, S., Souvatzis, P., Katsnelson, M.I., Ahuja, R., 2010. Dynamical stability of body center cubic iron at the Earth's core conditions. Proc. Natl. Acad. Sci. USA 107 (22), 9962–9964.

Mehl, M.J., Aguayo, A., Boyer, L.L., de Coss, R., 2004. Absence of metastable states in strained monatomic cubic crystals. Phys. Rev. B 70, 014101.

Mermin, N.D., 1965. Thermal properties of the inhomogeneous electron gas. Phys. Rev. 137, A1441–A1443.

Mikhaylushkin, A.S., Abrikosov, I.A., Belonoshko, A.B., Johansson, B., Simak, S.I., 2009. Instability of the body-centered tetragonal phase of iron under extreme conditions. Phys. Rev. B 79, 132106.

Monkhorst, H.J., Pack, J.D., 1976. Special points for Brillouin-zone integrations. Phys. Rev. B 13, 5188–5192.

Morelli, A., Dziewonski, A.M., Woodhouse, J.H., 1986. Anisotropy of the inner core inferred from PKIKP travel times. Geophys. Res. Lett. 13, 1545–1548.

Nguyen, J.H., Holmes, N.C., 2004. Melting of iron at the physical conditions of the Earth's core. Nature 427, 339–342.

Nose, S., 1984. A molecular dynamics method for simulations in the canonical ensemble. Mol. Phys. 52 (2), 255–268.

Perdew, J.P., Burke, K., Ernzerhof, M., 1996. Generalized gradient approximation made simple. Phys. Rev. Lett. 77, 3865.

Petigura, E.A., Howard, A.W., Marcy, G.W., 2013. Prevalence of Earth-size planets orbiting sun-like stars. Proc. Natl. Acad. Sci. USA 110, 19273–19278.

Pickard, C.J., Needs, R.J., 2009. Stable phases of iron at terapascal pressures. J. Phys. Condens. Matter 21, 452205.

Ping, Y., Coppari, F., Hicks, D.G., Yaakobi, B., Fratanduono, D.E., Hamel, S., Eggert, J.H., Rygg, J.R., Smith, R.F., Swift, D.C., Braun, D.G., Boehly, T.R., Collins, G.W., 2013. Solid iron compressed up to 560 GPa. Phys. Rev. Lett. 111, 065501.

Ross, M., Young, D.A., Grover, R., 1990. Theory of the iron phase diagram at Earth core conditions. J. Geophys. Res., Solid Earth 95, 21713–21716.

Ruban, A.V., Belonoshko, A.B., Skorodumova, N.V., 2013. Impact of magnetism on Fe under Earth's core conditions. Phys. Rev. B 87, 014405.

Sakai, T., Ohtani, E., Hirao, N., Ohishi, Y., 2011. Stability field of the hcp-structure for Fe, Fe–Ni and Fe–Ni–Si alloys up to 3 Mbar. Geophys. Res. Lett. 38 (9), L09302.

Seager, S., Kuchner, M., Hier-Majumder, C.A., Militzer, B., 2007. Mass–radius relationships for solid exoplanets. Astrophys. J. 669, 1279–1297.

Souvatzis, P., Eriksson, O., Katsnelson, M.I., Rudin, S.P., 2008. Entropy driven stabilization of energetically unstable crystal structures explained from first principles theory. Phys. Rev. Lett. 100, 095901.

Steinle-Neumann, G., Stixrude, L., Cohen, R.E., 1999. First-principles elastic constants for the hcp transition metals Fe, Co, and Re at high pressure. Phys. Rev. B 60, 791–799.

Steinle-Neumann, G., Stixrude, L., Cohen, R.E., Gulseren, O., 2001. Elasticity of iron at the temperature of Earth's inner core. Nature 413, 57–60.

Stixrude, L., 2012. Structure of iron to 1 Gbar and 40 000 K. Phys. Rev. Lett. 108, 055505.

Stixrude, L., Cohen, R.E., 1995. High pressure elasticity and of iron and anisotropy of Earth's inner core. Science 267, 1972–1975.

Stixrude, L., Cohen, R.E., Singh, D.J., 1994. Iron at high pressure: linearized-augmented-plane-wave computations in the generalized-gradient approximation. Phys. Rev. B 50, 6442–6445.

Tateno, S., Hirose, K., Ohishi, Y., Tatsumi, Y., 2010. The structure of iron in Earth's inner core. Science 330, 359–361.

Tateno, S., Hirose, K., Komabayashi, T., Ozawa, H., Ohishi, Y., 2012. The structure of Fe–Ni alloy in Earth's inner core. Geophys. Res. Lett. 39, L12305.

Vocadlo, L., 2007. Ab initio calculations of the elasticity of iron and iron alloys at inner core conditions: evidence for partially molten inner core? Earth Planet. Sci. Lett. 254, 227–232.

Vocadlo, L., Alfe, D., Gillan, M.J., Wood, I.G., Brodholt, J.P., Price, G.D., 2003. Possible thermal and chemical stabilization of body-centred-cubic iron in the Earth's core. Nature 424, 536–539.

Vocadlo, L., Wood, I.G., Gillan, M.J., Brodholt, J., Dobson, D.P., Price, G.D., Alfe, D., 2008. The stability of bcc-Fe at high pressures and temperatures with respect to tetragonal strain. Phys. Earth Planet. Inter. 170, 52–59.

Wang, F.M., Ingalls, R., 1998. Iron bcc–hcp transition: local structure from X-ray-absorption fine structure. Phys. Rev. B 57, 5647–5654.

Wang, J., Smith, R.F., Eggert, J.H., Braun, D.G., Boehly, T.R., Reed Patterson, J., Celliers, P.M., Jeanloz, R., Collins, G.W., Duffy, T.S., 2013. Ramp compression of iron to 273 GPa. J. Appl. Phys. 114, 023513.